

The influence of gravity on the steady propagation of a semi-infinite bubble into a flexible channel

Andrew L. Hazel and Matthias Heil

School of Mathematics, University of Manchester, Oxford Road, Manchester M13 9PL, United Kingdom

(Received 2 September 2007; accepted 15 July 2008; published online 25 September 2008)

Motivated by discrepancies between recent bench-top experiments [A. Juel and A. Heap, *J. Fluid Mech.* **572**, 287 (2007)] and numerical simulations [A. L. Hazel and M. Heil, *ASME J. Biomech. Eng.* **128**, 573 (2006)] we employ computational methods to examine the effects of transverse gravity on the steady propagation of a semi-infinite, inviscid air finger into a two-dimensional elastic channel filled with a Newtonian fluid. The special case of propagation in a rigid channel is also discussed in Appendix B. The coupled free-surface, fluid-structure-interaction problem is solved numerically using the object-oriented multiphysics finite-element library OOMPH-LIB. In the absence of gravity the relationship between the applied pressure and the propagation speed of the finger is nonmonotonic, with a turning point at small values of the propagation speed. We demonstrate that the turning point disappears when a modest gravitational force is applied and conjecture that it is this effect of gravity rather than any instability of the zero-gravity solution, as postulated in previous studies, that explains why the turning point has never been observed in experiments. At large propagation speeds, the presence of transverse gravity is shown to increase the pressure required to drive the air finger at a given speed, which is consistent with the observed discrepancies between previous zero-gravity simulations and the experimental results. Finally, we briefly discuss the possible implications of our results for the physiological problem of pulmonary airway reopening. © 2008 American Institute of Physics. [DOI: [10.1063/1.2982520](https://doi.org/10.1063/1.2982520)]

I. INTRODUCTION

We consider the steady propagation of a semi-infinite air finger into a two-dimensional elastic channel filled with a Newtonian fluid, a model problem motivated by the desire to understand the mechanisms underlying pulmonary airway reopening.

The airways of the lung are elastic vessels normally lined by a thin film of viscous fluid. The smaller airways are prone to a fluid-elastic instability that results in the collapse of the vessel wall and redistribution of the lining fluid. The end result is a blockage of the lumen, the air-conveying core of the airway.¹ Under normal physiological conditions, airway closure only occurs toward the end of forced expiration, and the blocked airways reopen during early inspiration. However, many pulmonary diseases, including respiratory distress syndrome, emphysema, and pulmonary edema, increase the likelihood of airway closure and, in addition, make it more difficult to reopen the collapsed vessels.^{2,3} If the airways remain closed for a significant fraction of the breathing cycle the efficiency of the lungs is reduced and gas exchange is compromised. Once occluded, therefore, the airways must be reopened as quickly as possible but without causing damage to the delicate lung tissue.

Airway reopening is believed to occur through the propagation of an air finger into the collapsed fluid-filled region, a mechanism that also occurs at the “first breath” when air displaces the fluid that fills the lungs of a newborn baby. Gaver *et al.*⁴ conducted the first experimental model study of airway reopening by considering the propagation of an air finger into a fluid-filled, thin-walled polyethylene tube.

One result of the experiments was a characterization of the propagation speed of the bubble, U , as a function of the applied bubble pressure p_b^* . As U decreased, p_b^* also decreased and appeared to approach a finite value as $U \rightarrow 0$, which was interpreted as the minimum pressure required to generate bubble motion: the yield pressure.

Subsequently, motivated by the large aspect ratio of the experimental system, Gaver *et al.*⁵ developed a two-dimensional model of steady airway reopening in the absence of gravitational forces and fluid inertia. The airway was modeled as an infinite channel with flexible walls under an applied axial tension and supported by linearly elastic springs. Inside the channel, it was assumed that an inviscid, semi-infinite air bubble at pressure p_b^* advanced at a constant speed U , displacing a Newtonian fluid with viscosity μ . The surface tension at the air-fluid interface was assumed to be a constant γ^* and the capillary number $\text{Ca} = \mu U / \gamma^*$ was used as a dimensionless measure of the propagation speed of the bubble.

In contrast to the experimental results, the model predicted a two-branch behavior in the relationship between the bubble speed and applied bubble pressure. At high speeds (large Ca), the bubble speed increased monotonically with applied bubble pressure, as observed experimentally. As the capillary number decreased, however, a minimum was reached below which the applied bubble pressure began to increase again, growing without bound as the speed tended to zero. The explanation for this behavior is that at low Ca a large volume of fluid is “pushed” ahead of the bubble tip and the system behaves as though the bubble was propagating

into a rigid channel but with the additional constraint that the film thickness around the bubble is set by the level of collapse far ahead of the bubble tip. In the rigid system, the ratio of film thickness to the channel width tends to zero as the capillary number decreases⁶ and thus, in order to conserve mass in the elastic system, the channel width, and hence the bubble pressure, must increase. The above argument is independent of the spatial dimension and, indeed, a similar two-branch behavior was also found in the equivalent three-dimensional model system: a semi-infinite bubble propagating into an elastic tube.⁷

Extensions to the two-dimensional model have examined the effects of surfactant, and hence nonuniform surface tension at the interface,⁸ fluid inertia,⁹ and the effects of the reopening process on the epithelial cells that line the airway walls.¹⁰ Halpern *et al.*¹¹ investigated the stability of the steady reopening process in the two-dimensional model and found that the low-Ca (pushing) branch was unstable when the bubble pressure or volume flux was prescribed. Halpern *et al.*¹¹ suggested that the instability of the pushing branch was the reason why it has not been observed in experiments.

More recently, Juel and Heap¹² conducted an experimental study of the reopening of a fluid-filled elastic tube with sufficiently thick walls that bending effects could not be neglected. A direct comparison of their experimental results with computational results from the three-dimensional model of Hazel and Heil¹³ revealed significant differences. The numerical results consistently underpredicted experimentally measured bubble pressures and, as in the experiments of Gaver *et al.*,⁴ there was no evidence of two-branch behavior in the experimental data. Moreover, the domain shapes were obviously affected by the presence of gravity in the experimental system, a physical effect that was neglected in the numerical simulations. On the basis of these observations, Juel and Heap¹² conjectured that gravitational effects were largely responsible for the difference between the two sets of results.

Motivated by Juel and Heap's¹² work, we wish to assess the effects of gravity on the system and, for simplicity, we shall perform our study with the two-dimensional model problem used in many previous investigations.

II. THE MODEL

A semi-infinite air bubble propagates at a constant speed U into a flexible channel containing an incompressible Newtonian fluid with density ρ and dynamic viscosity μ . The pressure within the bubble is p_b^* and the (constant) surface tension at the air-liquid interface is γ^* , see Fig. 1.

The channel walls are modeled by two prestressed elastic beams with thickness h and the walls are connected by linear springs with stiffness K_{spring}^* and natural length $2H$. The distance H is chosen to be our reference length scale and the problem is formulated in dimensionless Cartesian coordinates, $\mathbf{x}=(x_1, x_2)=\mathbf{x}^*/H$. Throughout this paper an asterisk is used to denote dimensional quantities, as opposed to their dimensionless equivalents. The treatment of the springs is conceptually different from that of previous models,^{5,9} in which the walls were supported externally by the linear

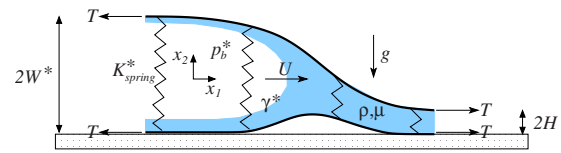


FIG. 1. (Color online) An air bubble with internal pressure p_b^* propagates at a constant speed U into a flexible channel formed by two beams connected by linear springs with stiffness K_{spring}^* and each prestressed by an axial force T . The channel contains incompressible Newtonian fluid with density ρ and dynamic viscosity μ and the surface tension at the air-liquid interface is a constant γ^* . Far ahead of the bubble tip, the channel width approaches the natural length of the springs, $2H$. Far behind the bubble tip, the channel opens to a width $2W^*$. The entire system is under the influence of a gravitational force with magnitude g that acts in a direction normal to the direction of bubble propagation and the system rests on a table located at $x_2=0$.

springs and the spring deformation was measured from a fixed coordinate ($x_2=1$). In the present context, the spring extension depends only on the distance between the two walls and not their absolute position in the global coordinate system, but the results of the two models are identical in the absence of gravity, see Fig. 6 below.

The bubble propagates in the positive x_1 direction and a constant gravitational body force with magnitude g acts on the system. We restrict attention to the case in which gravity acts in a direction normal to the direction of bubble propagation, as in the experiments. Far ahead of the bubble tip the fluid is at rest and the channel walls are separated by the natural length of the springs, $2H$. The external (pleural) pressure is chosen to be our reference pressure and is set to zero.

A. Fluid equations

We nondimensionalize the fluid velocity by the propagation speed of the bubble, $\mathbf{u}=\mathbf{u}^*/U$, and the fluid pressure on the viscous scale, $p=p^*/(\mu U/H)$. In a frame moving with the constant velocity of the bubble $(U, 0)$, the motion of the fluid is governed by the dimensionless steady Navier–Stokes equations

$$\text{Re } u_j \frac{\partial u_i}{\partial x_j} = -\frac{\partial p}{\partial x_i} + \frac{\partial}{\partial x_j} \left(\frac{\partial u_i}{\partial x_j} + \frac{\partial u_j}{\partial x_i} \right) + \frac{\text{Bo}}{\text{Ca}} k_i, \quad (1)$$

and the equation of continuity

$$\frac{\partial u_j}{\partial x_j} = 0. \quad (2)$$

The indices take the value $i=1, 2$ and we use the Einstein summation convention. The unit vector $\mathbf{k}=(0, -1)$ indicates the direction of the gravitational body force. The dimensionless groups in Eq. (1) are the Reynolds number $\text{Re}=\rho UH/\mu$ (the ratio of fluid inertial forces to viscous forces), the capillary number $\text{Ca}=\mu U/\gamma^*$ (the ratio of viscous forces to surface-tension forces), and the Bond number $\text{Bo}=\rho gH^2/\gamma^*$ (the ratio of gravitational forces to surface tension). The dimensionless grouping $\text{Bo}/\text{Ca}=\rho gH^2/\mu U$ that occurs in Eq. (1) is the ratio of gravitational forces to viscous forces.

B. Wall equations

The channel walls are modeled as prestressed elastic beams with thickness h , connected by linear springs with a spring stiffness K_{spring}^* . The undeformed system consists of two parallel beams separated by a vertical distance of 2 so that the springs are vertical and at their rest length.

Geometrically nonlinear beam theory is used to describe the deformation of the channel walls.¹⁴ Material lines normal to the undeformed centerline are assumed to remain unstretched and normal to the centerline during the deformation; hence, the position of the centerline is sufficient to describe the deformation of the beam. In the global Cartesian coordinate system, the undeformed centerlines are located at

$$\mathbf{R}^{[u]} = \mathbf{R}^{[u]*}/H = (\xi, 2) \quad (\text{upper wall}),$$

$$\mathbf{R}^{[l]} = \mathbf{R}^{[l]*}/H = (\xi, 0) \quad (\text{lower wall}),$$

and each centerline is parametrized by a single Lagrangian coordinate, $\xi = \xi^*/H$.

Working in a frame moving with the constant velocity of the bubble tip is equivalent to working in Lagrangian traveling-wave coordinates, $\zeta = \xi - t$, where $t = t^*U/H$. The position of the walls is then given by

$$\mathbf{R}^{[u]}(\xi, t) = \mathbf{R}^{[u]}(\zeta) = [r_1^{[u]}(\zeta), r_2^{[u]}(\zeta)],$$

$$\mathbf{R}^{[l]}(\xi, t) = \mathbf{R}^{[l]}(\zeta) = [r_1^{[l]}(\zeta), r_2^{[l]}(\zeta)].$$

The beams are prestressed by a force T , which generates an initial tension $\sigma_0^* = T/h$, and we assume that the additional strains induced by subsequent deformations are sufficiently small to justify the use of an incrementally linear constitutive equation. Thus, the dimensionless second Piola–Kirchhoff stress is given by $\sigma = \sigma^*/E = \sigma_0 + \epsilon$, where E is the incremental Young modulus (a linear approximation to the stress-strain relationship of the system after the application of the initial tension) and ϵ is the Green–Lagrange centerline strain, see Eq. (4).

The principle of virtual displacements states that external work generated by the virtual displacement of an elastic body must be equal to the virtual change in its strain energy. Under the above assumptions the variational principle for the upper wall takes the form

$$\begin{aligned} & \int_{-\infty}^{\infty} \left[(\sigma_0 + \epsilon^{[u]}) \delta \epsilon^{[u]} + \frac{1}{12} \left(\frac{h}{H} \right)^2 \kappa^{[u]} \delta \kappa^{[u]} \right] d\zeta \\ & = \frac{H}{h} \int_{-\infty}^{\infty} \mathbf{f}^{[u]} \cdot \delta \mathbf{R}^{[u]} \sqrt{(r_{1,\zeta}^{[u]})^2 + (r_{2,\zeta}^{[u]})^2} d\zeta \end{aligned} \quad (3)$$

after analytic integration through the thickness of the beam. The subscript ζ denotes differentiation with respect to the Lagrangian traveling-wave coordinate ζ . In the above, $\epsilon^{[u]}$ is the Green–Lagrange centerline strain

$$\epsilon^{[u]} = \frac{1}{2} \left(\left| \frac{\partial \mathbf{R}^{[u]}}{\partial \zeta} \right|^2 - 1 \right) = \frac{1}{2} [(r_{1,\zeta}^{[u]})^2 + (r_{2,\zeta}^{[u]})^2 - 1], \quad (4)$$

$\kappa^{[u]}$ is the dimensionless change of curvature of the centerline

$$\kappa^{[u]} = \frac{r_{2,\zeta\zeta}^{[u]} r_{1,\zeta}^{[u]} - r_{1,\zeta\zeta}^{[u]} r_{2,\zeta}^{[u]}}{\sqrt{(r_{1,\zeta}^{[u]})^2 + (r_{2,\zeta}^{[u]})^2}}, \quad (5)$$

and $\mathbf{f}^{[u]} = \mathbf{f}^{[u]*}/E$ is the nondimensional traction acting on the wall. Thus, the first two terms in Eq. (3) represent the change in internal strain energy due to stretching and bending, respectively, and the final term is the work done by the external load acting on the deformed wall. An analogous equation governs the deformation of the lower wall.

The load on the upper wall may be decomposed into the contribution from the fluid, the contribution from the linear springs, and the contribution from the mass of the wall, $\mathbf{f}^{[u]} = \mathbf{f}_{\text{fluid}} + \mathbf{f}_{\text{spring}} + \mathbf{f}_{\text{wall}}^{[u]}$. The spring at the material point ζ in the upper wall is connected to the material point ζ in the lower wall and remains attached to the same two points during the deformation; its position is thus described by the vector $\mathbf{D}_{\text{spring}}(\zeta) = \mathbf{R}^{[l]}(\zeta) - \mathbf{R}^{[u]}(\zeta)$, and

$$\mathbf{f}_{\text{spring}} = \frac{K_{\text{spring}}^* H (|\mathbf{D}_{\text{spring}}| - 2) \mathbf{D}_{\text{spring}}}{E \cdot 2 |\mathbf{D}_{\text{spring}}|}.$$

The load on the lower wall may be decomposed into four contributions, $\mathbf{f}^{[l]} = \mathbf{f}_{\text{fluid}} - \mathbf{f}_{\text{spring}} + \mathbf{f}_{\text{wall}}^{[l]} + \mathbf{f}_{\text{table}}$. The load from the linear springs acts in the opposite direction on the lower wall and there is an additional load due to the presence of a table, which is simulated by means of a large penalty force applied in the positive x_2 direction when the position of the lower wall falls below the location of the table at $x_2 = 0$. The value of the force used in the computations was typically $2000 K_{\text{spring}}^* H/E$ and it was confirmed that increasing the penalty force did not affect the results.

The fluid load on the walls is given by

$$\mathbf{f}_{\text{fluid}} = \frac{\mu U}{HE} \{ \rho \mathbf{N} - [\nabla \mathbf{u} + (\nabla \mathbf{u})^T] \cdot \mathbf{N} \}, \quad (6)$$

where \mathbf{N} is the unit normal to the deformed wall directed out of the fluid. The dimensionless grouping that multiplies the fluid load may be written as

$$\frac{\mu U}{HE} = \frac{\mu U}{\gamma^* HE} = \text{Ca } \gamma,$$

where $\gamma = \gamma^*/HE$ is the ratio of surface tension to the extensional stiffness of the channel walls.

The dimensional force due to the mass of the wall is obtained by integrating the force generated by the acceleration of the wall and the gravitational body force $\rho_w \mathbf{g}$ through the thickness of the wall and, so after nondimensionalization, we have

$$\mathbf{f}_{\text{wall}}^{[u/l]} = \left(\frac{\rho_w}{\rho} \right) \left(\frac{h}{H} \right) \gamma \left[\text{Re Ca } \frac{\partial^2 \mathbf{R}^{[u/l]}}{\partial \zeta^2} + \text{Bok} \right],$$

where ρ_w is the density of the wall. Typically the density ratio (ρ_w/ρ) will be of order 1, but we assume that h/H is sufficiently small that the contribution to the total force due to the mass of the wall may be neglected.

C. Boundary conditions

1. Air-liquid interface

In the moving frame, the kinematic condition on the air-liquid interface is a nonpenetration condition,

$$u_i n_i = 0, \quad (7)$$

where \mathbf{n} is the (outer) unit normal to the interface, and the dynamic boundary condition is

$$-pn_i + \left(\frac{\partial u_i}{\partial x_j} + \frac{\partial u_j}{\partial x_i} \right) n_j + \frac{1}{Ca} \kappa n_i = -p_b n_i, \quad (8)$$

where p_b is the dimensionless pressure of the air in the finger and $\kappa = \kappa^* H$ is the dimensionless curvature of the interface.

2. Channel walls

The no-slip boundary condition on the walls implies that the fluid velocity at the wall must be equal to the local wall velocity in the moving frame

$$\mathbf{u} = \begin{cases} -\frac{\partial \mathbf{R}^{[u]}}{\partial \zeta}, & \text{upper wall,} \\ -\frac{\partial \mathbf{R}^{[l]}}{\partial \zeta}, & \text{lower wall.} \end{cases} \quad (9)$$

3. “End” conditions

We truncate the computational domain at finite distances from the finger tip so that $\zeta_l \leq \zeta \leq \zeta_r$. The ends of the wall are fixed in the axial direction but remain free to move vertically except for the left-hand end of the lower wall, which is fixed at $\zeta = \zeta_l$ to prevent rigid body motions.

Sufficiently far from the finger tip in the moving frame, the fluid will have uniform velocity $u_1 = -1$, corresponding to zero velocity in a fixed frame and the fluid pressure will be hydrostatic, $\partial p / \partial x_2 = -Bo/Ca$. Applying these conditions directly requires the computational domain to be extremely long in order to avoid end effects, particularly at low capillary numbers. We find that accurate results can be obtained in smaller domains, however, if we assume that variations in the axial direction are gentle enough that a long-wavelength approximation is valid at the ends of the domain. Far ahead of the finger tip, the Navier–Stokes equations then reduce to a one-dimensional equation for the axial component of velocity,

$$\frac{\partial^2 u_1}{\partial x_2^2} = G, \quad (10)$$

subject to the no-slip boundary conditions at the walls. As $\zeta \rightarrow \infty$ the channel width approaches the rest length of the springs, 2, and the velocity approaches uniform (plug) flow $u_1 = -1$. The mass flux is thus $Q = -2$, which is imposed as a constraint at the finite distance $\zeta = \zeta_r$,

$$\int u_1|_{\zeta=\zeta_r} dx_2 = -2. \quad (11)$$

Constraint (11) is used to determine the unknown constant axial pressure gradient G in Eq. (10). The solution of Eq.

(10) is imposed as a Dirichlet condition for the axial velocity component and a traction consistent with the imposed velocity field is applied in the transverse direction.

Far behind the finger tip, the Navier–Stokes equations again reduce to a one-dimensional equation for the axial component of velocity,

$$\frac{\partial^2 u_1}{\partial x_2^2} = 0, \quad (12)$$

where the pressure gradient is assumed to be negligible and the boundary conditions are no-slip on the channel walls and the (natural) boundary condition on the air-liquid interface is

$$\frac{\partial u_1}{\partial x_2} = 0.$$

Again, the resulting axial velocity is imposed as a Dirichlet boundary condition and a consistent transverse traction is applied.

D. Numerical methods

The coupled set of equations that defines the system was solved numerically by the object-oriented multiphysics library OOMPH-LIB¹⁵ using a finite-element method. The wall equations were discretized by Hermite beam elements, in which the unknown positions are approximated by cubic polynomials within each element and the position and its derivative with respect to the Lagrangian coordinate are continuous between elements. The fluid equations were discretized using isoparametric Q_2P_{-1} finite elements,¹⁶ which use a bilinear approximation for the pressure and a biquadratic approximation for the global Cartesian coordinates and fluid velocity components. The velocity components and coordinates are continuous between elements, but the pressure may be discontinuous across element boundaries.

The fluid domain deforms in response to changes in the position of the channel walls and also to changes in the position of the air-liquid interface. The deformation is treated numerically by using a sparse node-update technique, a generalization of Kistler and Scriven’s¹⁷ “method of spines.” A continuous field of unit vectors, the spines, is defined and the nodes are positioned at fixed fractions of the “height” of the fluid domain measured in the direction of these spines, as shown in Fig. 2. In general, both the spine heights and spine directions vary as functions of the variables in the problem.

The fluid domain is split into three regions, see Fig. 2. In region III, $\zeta \geq 0$, there is no air-liquid interface. The spines are defined by the vectors that connect the points in the two channel walls at the same Lagrangian coordinate. In regions I and II, $\zeta < 0$, the presence of the interface must be taken into account. The interface position in the global Cartesian coordinate system is given by

$$\mathbf{R}_{fs}(s) = \mathbf{\Lambda}(s) + h(s)\mathbf{S}(s),$$

where s is a surface coordinate. Here, $\mathbf{\Lambda}(s)$ is a reference surface defined by the channel walls in regions I and II and the straight line that connects the points $\zeta = 0$ in each wall (the dividing line between regions II and III); $h(s)$ is the distance of the interface from the reference surface and $\mathbf{S}(s)$

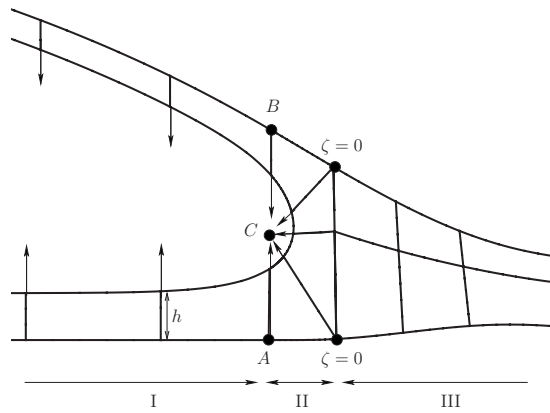


FIG. 2. Illustration of the spine-based, node-update technique used to deform the fluid domain in response to changes in the positions of the channel walls and the air-fluid interface. In region III, the spines are vectors that connect points at the same Lagrangian coordinate in the two channel walls. In region II, the spines are directed from the channel walls, or the line connecting the material points at $\zeta=0$, to the point C. In region I, the spines are oriented vertically.

is the field of spines. In contrast to the situation in region III where the chosen distance can be determined from the wall positions, the distance $h(s)$ is an unknown in the problem. In region II, the spines are all directed to a fixed point, C, a chosen fraction of the distance between two specified points on the channel walls, A and B in Fig. 2. In region I, the spines are vertical and directed toward the center of the channel.

The unknown function $h(s)$ is approximated by piecewise quadratic polynomials and the resulting discrete values are found from the weak form of kinematic boundary condition (7). The dynamic boundary condition (8) is incorporated into the weak form of the fluid momentum equation on integration by parts.¹⁸ Finally, the translational invariance of the problem is removed by fixing the position of the finger tip, a constraint that is used to determine the unknown bubble pressure.

The coupled system described above is assembled and solved by a fully coupled (monolithic) Newton method. A suitable initial guess is obtained by solving an approximation to the problem of bubble propagation in a rigid channel, achieved by setting K_{spring}^* to a high value, and replacing boundary conditions (10) and (11), applied far ahead of the finger tip, by $u_2=0$ and $p=-\text{Bo}/\text{Ca} x_2$. An initial bubble shape of two parallel lines connected by a semicircular cap is sufficient to obtain a converged solution at $\text{Ca}=0.05$. Next, the boundary conditions far ahead of the finger tip are changed back to Eqs. (10) and (11), but the (unrestricted) flux from the converged “rigid” solution is applied as the right-hand side in constraint (11); G is then computed as part of the next solution. From this “second” solution simple parameter continuation is used to extend the computations to the desired regions of parameter space.

In typical computations, the computational domain extended from $-300 \leq \zeta \leq 150$ and the system consisted of approximately 50 000 degrees of freedom. Code validation involved a comparison with the symmetric, zero-Bond-number calculations of Heil,⁹ see Figs. 6 and 10 below, and further

validation was provided by a high-resolution study (approximately 105 000 degrees of freedom) for nontrivial Bond and Reynolds numbers. The resulting bubble pressures at $\text{Ca}=2$, $\text{Bo}=0.5$, and $\text{Re}=15$, corresponding to the extremal point in Fig. 10(b), differ by less than 0.2%.

III. RESULTS

Although simplified, our model involves a large number of dimensionless parameters. In the interest of brevity, we shall concentrate on the effects of varying the Bond number $\text{Bo}=\rho g H^2/\gamma^*$ (the ratio of gravitational to surface-tension forces), which is estimated to lie in the range $0.08 \leq \text{Bo} \leq 0.12$ for the experiments of Gaver *et al.*⁴ and Perun and Gaver;¹⁹ in contrast, $\text{Bo} \approx 1$ in the experiments of Juel and Heap.¹²

Unless stated otherwise, the results are obtained using the same parameter values as Heil,⁹ which, in turn, correspond to those of the “basic state” defined by Gaver *et al.*⁵ The ratio of the wall tension to surface tension is

$$\eta = \frac{T}{\gamma^*} = \frac{\sigma_0^* h}{\gamma^*} = \frac{\sigma_0 h}{\gamma H} = 100,$$

and the ratio of spring stiffness to surface tension is

$$\Gamma = \frac{K_{\text{spring}}^* H^2}{\gamma^*} = 0.5.$$

The ratio of surface tension to extensional stiffness of the wall is $\gamma=10^{-7}$, and the wall thickness h/H is 5×10^{-4} , which ensures that bending effects are weak and that the mass of the channel walls can be neglected.

The effects of varying the parameters, η , Γ , γ , and h/H are essentially unaffected by the inclusion of gravity and are comprehensively discussed by Gaver *et al.*⁴ and Heil.⁹

A. Gravitational effects

The most dramatic effect of gravity is its influence on the shape of the domain. Figure 3 shows the domain shapes, streamlines, and fluid pressure contours at a fixed capillary number, $\text{Ca}=2.5$, as the Bond number is increased. For $\text{Bo}=0$, the system is symmetric and the results are in agreement with previous calculations.^{5,9} The fluid pressure is approximately uniform across the channel and the lowest pressure is attained in a “neck” region just ahead of the bubble tip. For nonzero Bond numbers, the symmetry is broken by the presence of gravity and the bubble is noticeably asymmetric with an approximately horizontal lower surface. The lower channel wall drops onto the table apart from the neck region, where the fluid pressure is sufficiently negative to lift the wall above the table. As the Bond number increases, the gravity-induced vertical pressure gradient increases and the resulting increase in fluid pressure at the lower wall pushes the wall onto the table. The neck region is still evident at the upper wall, however, where the fluid pressure remains negative.

Along with the changes in domain shape, the increase in gravitational forces causes a change in the pressure field from a predominantly horizontal viscous pressure gradient to

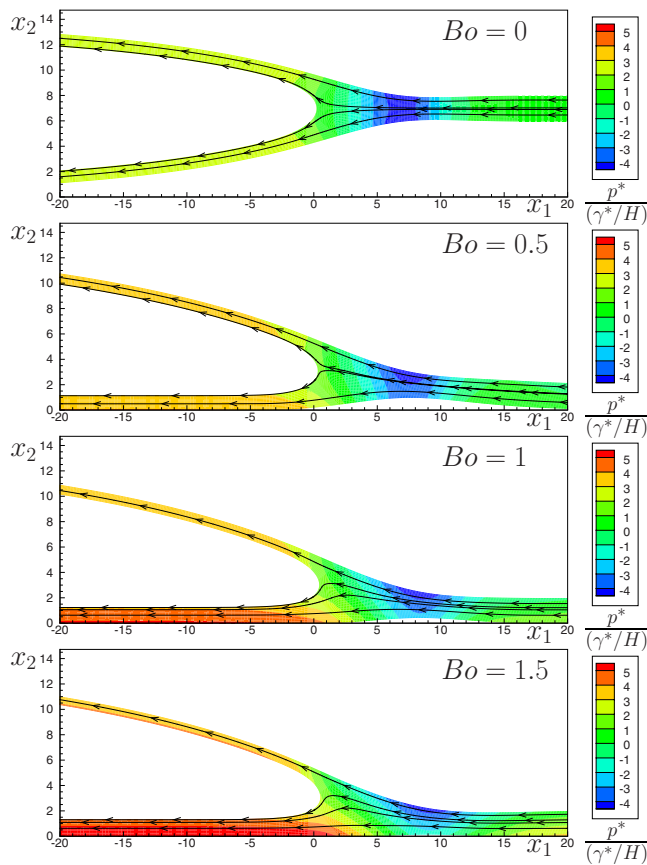


FIG. 3. (Color online) Contours of fluid pressure and streamlines at a fixed capillary number, $Ca=2.5$, for Bond numbers $Bo=0, 0.5, 1,$ and 1.5 .

a predominantly vertical “hydrostatic” pressure gradient. In terms of the overall behavior of the system, however, the most important effect is the buoyant rise of the bubble within the channel. This effect is more clearly presented in Fig. 4, which shows the vertical thickness of the upper and lower fluid films far behind the bubble tip plotted against the Bond number for varying capillary numbers. At $Bo=0$, the system

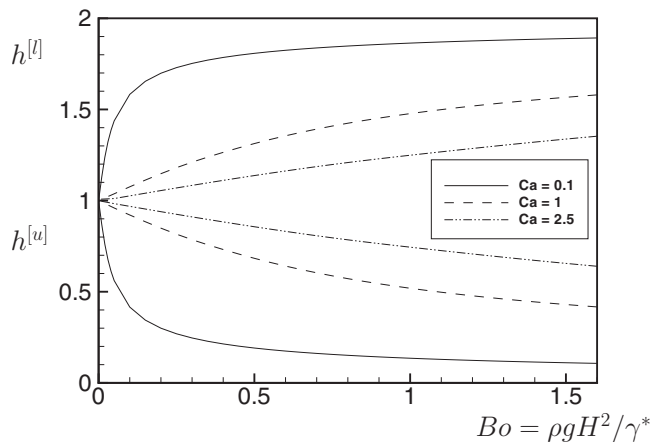


FIG. 4. The vertical height of the fluid films deposited on the upper, $h^{[u]}$ (lower lines), and lower, $h^{[l]}$ (upper lines), channel walls measured at $\zeta=\zeta_l$ plotted as a function of the Bond number. The results are shown at three different capillary numbers, $Ca=0.1, 1,$ and 2.5 . In the absence of gravity, the system is symmetric and $h^{[u]}=h^{[l]}=1$.

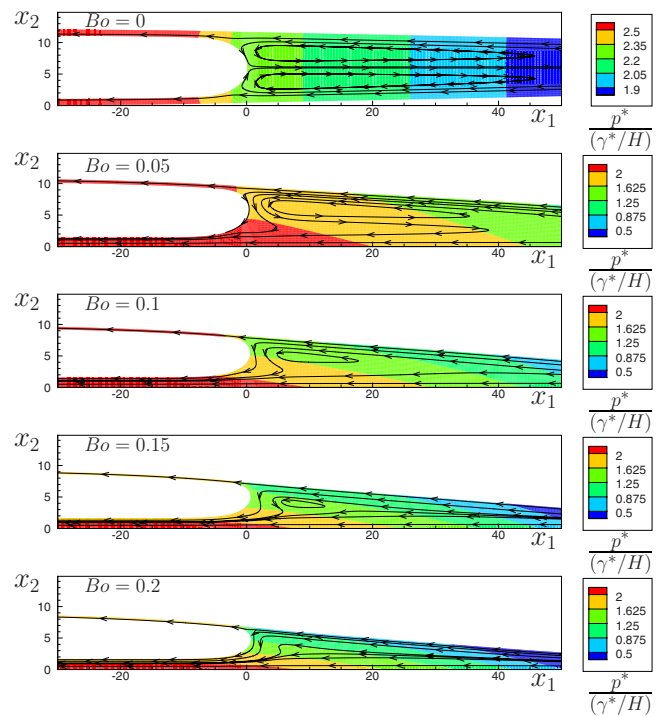


FIG. 5. (Color online) Contours of fluid pressure and streamlines at a fixed capillary number, $Ca=0.1$, for Bond numbers $Bo=0, 0.05, 0.1, 0.15,$ and 0.2 .

is symmetric and both films are of thickness 1. As the Bond number increases, the lower film thickens as the bubble rises and because mass conservation implies that the sum of the two film thicknesses must remain the same far behind the bubble tip, the upper film thins, see Fig. 4. The influence of gravity in the Navier–Stokes equations (1) is represented by the term $(Bo/Ca)\mathbf{k}$. The system will, therefore, be more sensitive to changes in the Bond number at small capillary numbers. The rapid change in film thickness with Bond number at $Ca=0.1$ is a direct result of this sensitivity.

The extreme sensitivity of the system to changes in the Bond number at small capillary numbers is also demonstrated in Fig. 5, which shows channel shapes, streamlines, and pressure contours at a smaller capillary number of $Ca=0.1$. The buoyant rise of the bubble is much more evident in Fig. 5 than in Fig. 3. At $Bo=0$, the system is symmetric and a large volume of fluid is pushed ahead of the bubble tip. Three stagnation points are located on the bubble surface: one on the channel’s centerline and one at the end of each of the two recirculation regions. Again, the inclusion of the gravitational body force breaks the symmetry of the system and the central and lower stagnation points move toward one another with a consequent increase in the size of the upper recirculation region. By $Bo=0.05$ these two stagnation points have merged, which causes the two recirculation regions ahead of the tip to be replaced by a single one in the upper half of the channel. The angle of the upper channel wall to the horizontal increases and a vertical pressure gradient becomes noticeable. As the Bond number increases further, the

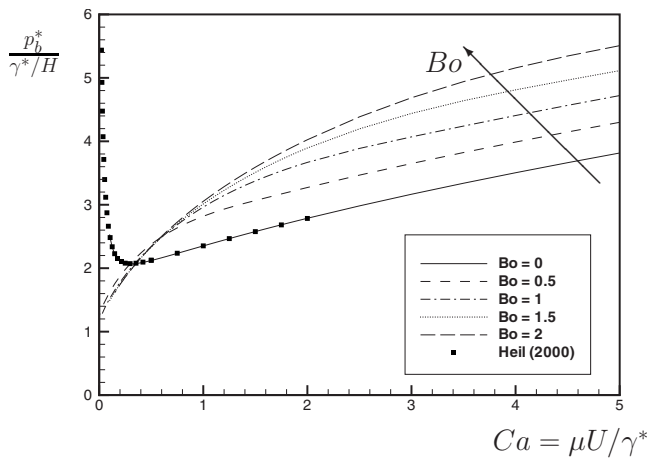


FIG. 6. The bubble pressure p_b plotted against capillary number Ca for Bond numbers $Bo=0, 0.5, 1, 1.5,$ and 2 , increasing in the direction of the arrow. The data from the symmetric calculations of Heil (Ref. 9) for $Bo=0$ are shown as markers.

bubble rises toward the upper channel wall, and the recirculation region becomes smaller, having disappeared completely by $Bo=0.2$.

The sequence of changes in the topology of the flow field with increasing Bo are consistent with the trends observed by Zheng *et al.*²⁰ who studied the propagation of liquid plugs in rigid channels. They also found stagnation points on the advancing interface at $Bo=0$ and observed that the lower two moved closer together as the Bond number increased. The Bond numbers at which the two stagnation points merge are rather higher than in our study, however.

We now consider the behavior of the system under variations in the capillary number. Figure 6 shows the bubble pressure, on the capillary scale, plotted against the capillary number for five different Bond numbers, $Bo=0, 0.5, 1, 1.5, 2$. The data of Heil⁹ for the case $Bo=0$ are reproduced on the figure and are in excellent agreement with our results; the maximum relative error between his computations and ours is less than 0.1%.

At high values of the capillary number, the buoyancy term in the Navier–Stokes equations becomes negligible, see above, and gravity has no dynamic effect on the system. Nonetheless, the presence of the hydrostatic pressure gradient means that the fluid pressure will drop through the thickness of the film between the upper surface of the bubble and the upper channel wall. Thus, in order to achieve the same transmural pressure across the upper channel wall in the presence of gravity, the bubble pressure must increase by $Bo h^{[u]}$, where $h^{[u]}$ is the vertical thickness of the upper film. At high values of Ca , the shape of the fluid domain becomes approximately independent of the Bond number and $h^{[u]}$ approaches a constant, ultimately reaching the value of 1. Hence, the p_b - Ca curves are simply shifted vertically by a constant amount. Naturally, as Bo increases, the value of Ca at which the curves become parallel increases.

As the capillary number decreases, the bubble pressure decreases. A striking feature of the results at nonzero Bond number, compared to those at $Bo=0$, is the absence of the turning point and the consequent disappearance of the two-

branch behavior. The bubble pressures decrease monotonically and appear to approach finite nonzero values as $Ca \rightarrow 0$, in agreement with the experimental results.^{4,12}

In order to explain this behavior, we exploit the fact that at small capillary numbers a large volume of fluid is pushed ahead of the finger tip and the slope of the channel walls is small, so that the finger propagates into an approximately parallel-walled channel. Therefore, we expect the system's behavior to be similar to that of a long bubble propagating into a rigid parallel-walled channel with the same width, $2W^*$. Bretherton's⁶ analysis of that problem demonstrated that at zero Bond number the relative film thickness (the film thickness divided by the channel width, h^*/W^*) tends to zero as $Ca \rightarrow 0$. This is because, in the absence of gravity, the air-liquid interface at the finger tip approaches the static equilibrium configuration in which a semicircular cap spans the entire channel. In the elastic system, mass conservation requires that the absolute film thickness must remain constant as the capillary number decreases. Because $h^*/W^* \rightarrow 0$ as $Ca \rightarrow 0$ the film thickness can only remain constant if the channel inflates, which is the explanation for the development of the second branch in the p_b - Ca curve at $Bo=0$.

Jensen *et al.*²¹ determined the static equilibrium configuration of an air-liquid interface in a rigid channel in the presence of transverse gravity. They found that when the Bond number (based on the channel half-width) exceeds 1, it is possible to obtain solutions in which the upper surface of the bubble meets the upper wall but the lower surface remains above the lower wall. The dimensionless width of these "floating" static bubbles was found to be $W_b^*/H = 2\sqrt{1/Bo}$, where H is equal to the channel half-width; see Appendix A for a summary of their theory. An alternative interpretation of their result is that for a fixed Bond number once the channel width is large enough, $2W = 2W^*/H > 2\sqrt{1/Bo}$, a film with finite thickness remains on the lower wall as $Ca \rightarrow 0$. Thus, in the elastic system, provided that $W > 1/\sqrt{Bo}$, mass can be conserved at a finite bubble pressure in the limit $Ca \rightarrow 0$. Moreover, no matter how small the Bond number the channel width can always be increased beyond $1/\sqrt{Bo}$; in other words, once gravitational forces are included the bubble pressure remains finite as $Ca \rightarrow 0$. For small Bo , the channel must increase in width at low Ca before it exceeds $1/\sqrt{Bo}$ and so a second branch is still present. If W remains greater than $1/\sqrt{Bo}$ for all capillary numbers, however, then a second branch will never develop, as seen in Fig. 6. We can obtain an approximation for the value Bo_c at which the second branch disappears by assuming that the minimum possible channel width is the minimum channel width in the absence of gravity, $W_{\min} \approx 5$, corresponding to $p_{b \min} \approx 2$. Thus, the largest Bond number at which the second branch can occur is determined by the condition $W_{\min} \approx 5 \approx 1/\sqrt{Bo_c}$ and so $Bo_c \approx 1/25 = 0.04$.

In order to examine the validity of this approximation Fig. 7 shows the bubble pressures plotted against the capillary number for small values of the Bond and capillary numbers. There is still evidence of a pushing branch at $Bo=0.05$, but it appears to have vanished by $Bo=0.07$. The simulation results are presented for $Ca \geq 0.1$, a regime in

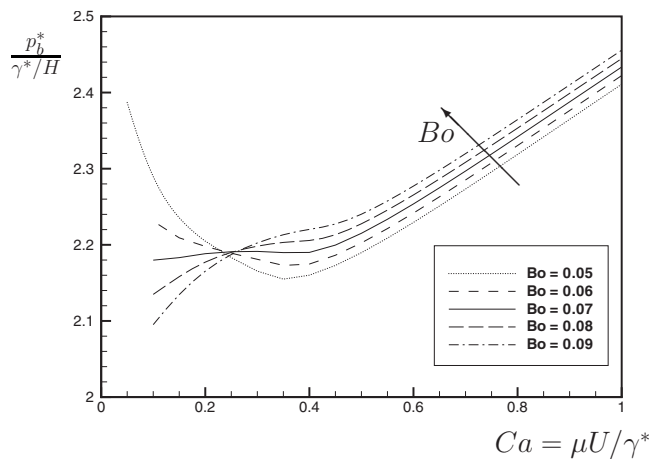


FIG. 7. The bubble pressure p_b plotted against capillary number Ca for Bond numbers $Bo=0.05, 0.06, 0.07, 0.08,$ and 0.09 , increasing in the direction of the arrow. Calculations based on bubble propagation in rigid channels predict the disappearance of the pushing branch at $Bo \approx 0.07$.

which our standard spatial resolution is sufficient to resolve the flow field completely. The extreme thinning of the fluid films at even lower capillary numbers would require a higher spatial resolution, but regardless of the spatial resolution chosen it would never be possible to continue the computations to $Ca=0$. Hence, we cannot rule out the possibility that pushing behavior could develop at very low capillary numbers. Nonetheless, the prediction of Bo_c from the static result in a rigid, parallel-walled channel is surprisingly close to the value at which the turning point seems to disappear.

A yet more accurate approximation for Bo_c can be obtained by making use of the fact that W_{\min} occurs at a finite capillary number, $Ca \approx 0.3$. An estimate for Bo_c was found by modifying the numerical approach so that it applied to the problem of bubble propagation in a rigid, parallel-walled channel, see Appendix B. At $Ca=0.3$, for a given Bond number, a Newton method was used to find the channel width at which the total dimensionless flow rate was 2, as required to conserve mass in the elastic-walled problem. The Bond number for which the calculated channel width first exceeded $1/\sqrt{Bo}$ was found to be $Bo_c \approx 0.07$, in excellent agreement with the numerical results above. Indeed, it is remarkable that the agreement is quite so good given that the inclusion of gravity in the problem means that the upper channel wall is generally not parallel to the lower wall, see Fig. 5. Note, however, that the channel walls become closer to parallel as the spring stiffness is increased and the results of the elastic system approach the predictions of the rigid, parallel-wall simulations with increasing accuracy.

B. Fixed lower wall

Our simulations show that the inclusion of gravity in the system has two main effects: (i) the overall symmetry of the domain is broken because the lower wall rests on the table and (ii) the symmetry of the bubble's position within the channel is broken because the bubble rises toward the upper wall. We attempt to disentangle these two effects by fixing the lower channel wall at $x_2=0$. We note that this problem, in

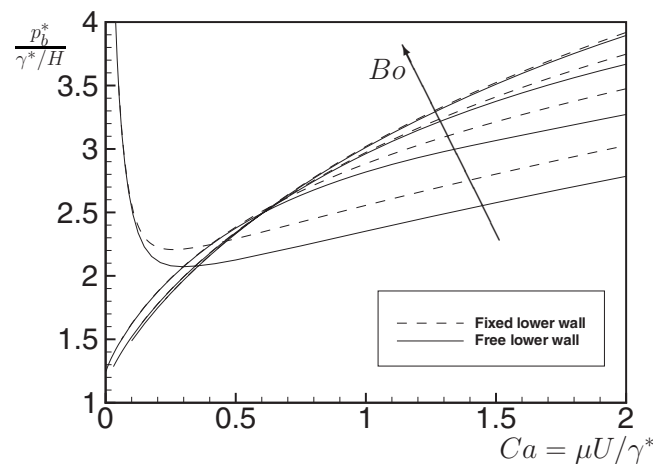


FIG. 8. The bubble pressure p_b plotted against capillary number Ca for Bond numbers $Bo=0, 0.5, 1,$ and 1.5 , increasing in the direction of the arrow, in the case when the lower channel wall is fixed at $x_2=0$ (dashed lines) and the case when the lower channel wall is free (solid lines).

the absence of gravity, was also considered by Jensen *et al.*²² who proposed that a no-slip boundary on the lower wall would be a better model of the experimental system of Perun and Gaver.¹⁹

Figure 8 presents p_b - Ca curves for fixed and free lower channel walls at $Bo=0, 0.5, 1,$ and 1.5 . In general, fixing the lower channel wall leads to a higher bubble pressure at a given capillary number. At low capillary numbers, gravitational effects are dominant and the channel wall rests on the table even when not fixed; hence the results are identical in the two cases. As the capillary number increases, the unfixed wall can lift off the table and the different geometries in the two cases leads to the differences in bubble pressures. The precise capillary number at which the results begin to differ increases with increasing the Bond number because the unconstrained wall remains on the table for a greater range of capillary numbers as the gravitational force increases.

In the case when the lower wall is fixed, the two-branch behavior is still evident at $Bo=0$, confirming that the disappearance of the second branch is a consequence of the buoyant rise of the bubble within the channel. The breaking of the symmetry of the domain causes a modest increase in bubble pressure but does not lead to a qualitative change in the behavior of the system.

C. Inertial effects

In a typical experimental study the bubble pressure is measured at a number of different flow rates and the Reynolds number will vary because it depends on the propagation speed of the bubble, U . The dimensionless parameter formed by the ratio of the Reynolds and capillary numbers,

$$\frac{Re}{Ca} = \frac{\rho \gamma^* H}{\mu^2},$$

is a material parameter, however, and remains constant for any system that consists of a given fluid and a given elastic channel. Thus, we shall use Re/Ca rather than Re to quantify the effects of fluid inertia on the system.

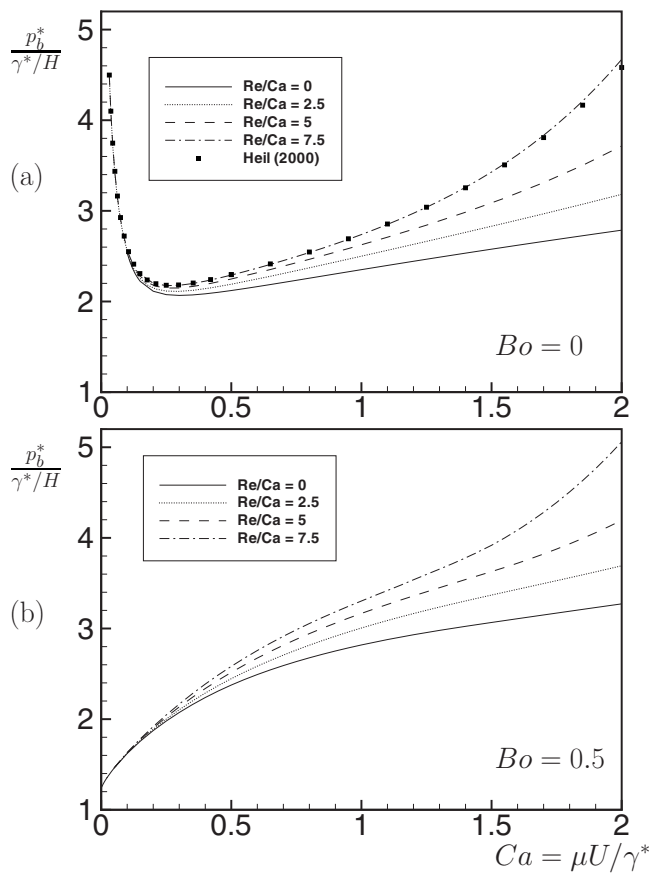


FIG. 9. The bubble pressure p_b plotted against capillary number Ca for fixed Bond numbers (a) $Bo=0$ and (b) $Bo=0.5$ for four different values of $Re/Ca=0, 2.5, 5,$ and 7.5 . In (a) the results of Heil (Ref. 9) for $Bo=0$ and $Re/Ca=7.5$ are shown as markers.

Figure 9 shows the p_b - Ca traces for different values of the material parameter Re/Ca for $Bo=0$ and $Bo=0.5$. The results in the absence of gravity, Fig. 9(a), have been previously presented, see Heil's⁹ Fig. 6, and we compare the two sets of results at $Re/Ca=7.5$. At the very highest capillary numbers, the results differ slightly which we attribute to Heil's⁹ use of lubrication theory in the regions $-300 \leq \zeta \leq -40$ and $80 \leq \zeta \leq 150$.

In both cases, $Bo=0$ and $Bo=0.5$, the main effect of fluid inertia is to increase the bubble pressure required to drive the system at a given capillary number, an effect that becomes more pronounced as the capillary number, and hence the Reynolds number, increases. At high Ca , the buoyancy term in the Navier–Stokes equations is negligible and the change in bubble pressure caused by increasing Re is unaffected by the Bond number. At low Ca , the Reynolds numbers are very small and fluid inertia does not significantly alter the behavior of the system, but it is precisely in this regime that gravitational effects are most important because the hydrostatic pressure gradient is much greater than the viscous pressure drop. Thus, the effects of fluid inertia and gravity are confined to different ranges of the capillary number and are essentially independent.

Figure 10 shows the effect of fluid inertia on the system at $Ca=2$ and $Bo=0.5$. The introduction of fluid inertia causes an increase in the amplitude of a damped oscillatory eigen-

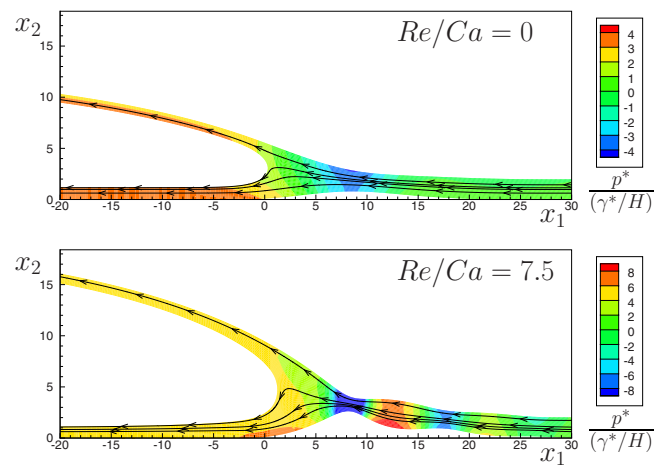


FIG. 10. (Color online) Contours of fluid pressure on the surface-tension scale and streamlines for $Ca=2$, $Bo=0.5$, and $Re/Ca=0$ and 7.5 . A damped oscillatory wall displacement field can be seen when $Re/Ca=7.5$.

function of the wall displacement field, the first minimum of which can be identified with the neck region in the case $Re/Ca=0$. The increase in amplitude is consistent with the Bernoulli effect, which only applies in the presence of fluid inertia. In the neck region, the channel is at its narrowest and the constant flow rate means that the fluid velocity must increase locally. The Bernoulli effect causes a decrease in fluid pressure, in response to the increased fluid velocity, and the low fluid pressure “pulls” the channel walls inwards. The channel width far ahead of the bubble tip remains at the same prescribed value, however, leading to an increase in amplitude of the oscillations.

The explanation for the increase in bubble pressure with fluid inertia has been given by Heil⁹ and Hazel and Heil¹³ who observed the same effect in a three-dimensional model of the system. In essence, the change in the geometry of the fluid domain leads to an increase in the size of the region in which the flow is spatially nonuniform, causing an increase in the viscous dissipation and hence an increase in the bubble pressure required to drive the finger at a given speed. Moreover, the Bernoulli effect will become more significant as the bubble speed increases, explaining the rapid increase in bubble pressure with capillary number for relatively modest values of Re/Ca .

IV. CONCLUSIONS

The main motivation of the present work has been to assess whether the inclusion of gravitational forces can account for the differences between numerical simulations and bench-top experiments modeling the airway reopening process. For simplicity, we considered a two-dimensional model problem: the steady propagation of a semi-infinite air finger into an elastic channel filled with a Newtonian fluid.

We find that the introduction of gravity causes a qualitative change in the behavior of the system, namely, the absence of a turning point in the p_b - Ca curve. This change is a consequence of the buoyant rise of the bubble, which ensures that mass can be conserved at a finite channel width in the limit $Ca \rightarrow 0$, no matter how small the Bond number. In our

two-dimensional model, we find that once the Bond number exceeds a threshold value ($\text{Bo}_c \approx 0.07$ for the parameter values chosen in our simulations) the bubble pressure decreases monotonically with decreasing capillary number for the range of capillary numbers considered in our study ($0.1 \leq \text{Ca} \leq 5$). In this regime, the bubble pressure appears to tend to a finite limit as $\text{Ca} \rightarrow 0$, the yield pressure, in agreement with experimental observations.^{4,12} In their experiments, Gaver *et al.*⁴ estimated that the yield pressure was approximately $8\gamma^*/W^*$. Using data from simulations at $\text{Bo}=0.1$, corresponding to the middle of the experimental range of Bond numbers, we estimate the yield pressure to be $9.4\gamma^*/W^*$, in close agreement with the experimental result. Hence, the fact that two-branch behavior has never been observed experimentally is more likely to be a consequence of the influence of gravity rather than the lack of stability of the low-Ca (pushing) branch *per se*.

The influence of the dimensionless spring stiffness Γ on the threshold value of the Bond number Bo_c may be estimated by using the (linear) relationship between bubble pressure and channel width in the absence of gravity: $p_b = \Gamma(W - 1)$. Using the width of the floating static bubble to estimate the critical value of the Bond number, as in Sec. III, gives $W_{\min} = p_{b \min}/\Gamma + 1 \approx 1/\sqrt{\text{Bo}_c}$ and so $\text{Bo}_c \approx (p_{b \min}/\Gamma + 1)^{-2}$, suggesting that Bo_c decreases with decreasing Γ provided that $p_{b \min}$ does not also decrease at a faster rate. Figure 14 of Gaver *et al.*⁵ shows that $p_{b \min} \approx 3.3$ for $\Gamma=1$ and $p_{b \min} \approx 0.8$ for $\Gamma=0.1$, so $\text{Bo}_c \approx 0.054$ for $\Gamma=1$, $\text{Bo}_c \approx 0.04$ for $\Gamma=0.5$ (see Sec. III), and $\text{Bo}_c \approx 0.012$ for $\Gamma=0.1$. Thus, we expect that Bo_c will decrease with decreasing spring stiffness presumably because the channel is more inflated at a given bubble pressure when the spring stiffness is reduced.

The effects of gravity on the fluid are most noticeable at low capillary numbers (low bubble speeds), when the viscous pressure gradient is small in comparison to the gravitational (hydrostatic) pressure gradient. For sufficiently large capillary numbers the effect of gravity is essentially passive, leading to an increase in the bubble pressure to compensate for the hydrostatic pressure drop through the thickness of the fluid film deposited on the upper wall. In contrast, the effects of fluid inertia are of greatest importance at high capillary numbers (large bubble speeds) and are negligible at low speeds. Thus, the effects of fluid inertia and gravitational forces are effectively independent but both cause an increase in the required bubble pressure to drive the bubble at a given speed for sufficiently large capillary numbers. The inclusion of a finite wall mass would lead to a further slight increase in the bubble pressure to compensate for the additional load on the wall.

The detailed behavior of the three-dimensional system will differ from our two-dimensional model. The development of transverse draining flows, for example, is not possible in two dimensions. Nonetheless, the buoyant rise of the bubble and the consequent absence of the two-branch behavior will be a feature of the system for sufficiently large Bond numbers. We believe, therefore, that the absence of gravity in our previous simulations¹³ is indeed the reason for the discrepancy between the computational and experimental results reported by Juel and Heap.¹²

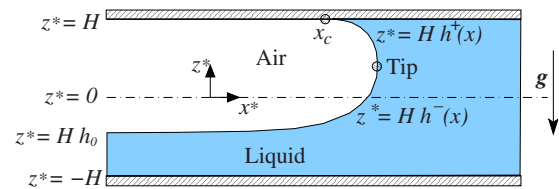


FIG. 11. (Color online) Sketch of a floating static bubble in a rigid channel with width $2H$. At x_c , the air-liquid interface meets the upper wall at zero contact angle; far behind the tip the air-liquid interface becomes horizontal at a vertical location $z = z^*/H = h_0$. The interface is divided into two regions, above and below the tip, parametrized by the functions $z = h^+(x)$ and $z = h^-(x)$, respectively.

Based on the stability analysis of Halpern *et al.*,¹¹ Hazel and Heil¹³ concluded that stable steady reopening of the airways of the lung in the absence of gravity would require such high speeds that it would be impractical. The present results indicate that in conditions of weak gravity, however, stable steady reopening of collapsed airways is possible at low speeds and at relatively low pressures, which would minimize damage to the airway walls. The application of our results to the situation *in vivo* must, of course, be treated with some caution, but we believe that the buoyant rise of the bubble is sufficiently generic that it will apply to the situation in the lungs.

ACKNOWLEDGMENTS

The authors would like to thank the anonymous referees for their helpful comments on an earlier revision of the present work. In particular, the authors would like to thank one of the referees for suggesting (and doing) the analysis to investigate the variation in Bo_c with Γ and for suggesting the inclusion of Appendixes A and B.

APPENDIX A: THE THEORY OF JENSEN *ET AL.* FOR STATIC AIR-LIQUID INTERFACES IN A RIGID CHANNEL UNDER A TRANSVERSE GRAVITATIONAL FIELD

We summarize the method of Jensen *et al.*²¹ used to determine the width of a static floating bubble in a rigid channel under a transverse gravitational field.

Consider a two-dimensional channel defined by the region $-\infty \leq x^* \leq \infty$ and $-H \leq z^* \leq H$, see Fig. 11. The channel is occupied by a viscous fluid with density ρ at rest under hydrostatic pressure $p_0^* - \rho g z^*$, where p_0^* is the pressure at the center of the channel, $z^* = 0$, and g is the acceleration due to gravity. An interface with constant surface tension γ^* separates the viscous fluid from an air finger with negligible viscosity and density under internal pressure p_b^* . A normal stress balance at the interface gives

$$-p_b^* + \gamma^* \kappa^* = -p_0^* + \rho g z^*,$$

where κ^* is the curvature of the interface. Nondimensionalizing lengths on the channel half-width H and pressures on the capillary scale γ^*/H , the stress balance becomes $\Delta p = -\text{Bo}z + \kappa$, where $\Delta p = p_b - p_0$ and $\text{Bo} = \rho g H^2 / \gamma^*$. In order to represent the interface by single-valued functions, Jensen *et al.*²¹ parametrized the location of the interface above and

below the bubble tip by the functions $z=h^+(x)$ and $z=h^-(x)$, respectively. The pressure jump across the air-liquid interface using such a parametrization is then given by

$$\Delta p = -Boh^+ - \frac{h_{,xx}^+}{[1 + (h_{,x}^+)^2]^{3/2}} \quad (\text{upper region}), \quad (\text{A1a})$$

$$\Delta p = -Boh^- + \frac{h_{,xx}^-}{[1 + (h_{,x}^-)^2]^{3/2}} \quad (\text{lower region}), \quad (\text{A1b})$$

where a comma is used to denote (ordinary) differentiation. Multiplying each equation by $h_{,x}^\pm$ and integrating gives

$$\Delta p h^\pm + \frac{1}{2}Bo(h^\pm)^2 = \pm \frac{1}{[1 + (h_{,x}^\pm)^2]^{1/2}} + C^\pm. \quad (\text{A2})$$

In the upper region, the interface meets the wall at zero contact angle at an unknown location x_c , so $h^+=1$ and $h_{,x}^+=0$ at $x=x_c$. At this location, Eq. (A2) becomes

$$\Delta p + 1/2Bo = 1 + C^+. \quad (\text{A3})$$

In the lower region, the interface becomes horizontal and remains at an unknown distance h_0 from the wall, so $h^-=h_0$ and $h_{,x}^- \rightarrow 0$ as $x \rightarrow -\infty$. Equation (A2) becomes

$$\Delta p h_0 + 1/2Boh_0^2 = -1 + C^- \quad (\text{A4})$$

or, using normal stress balance (A1b) directly,

$$\Delta p = -Boh_0 \quad (\text{A5})$$

because $h_{,xx}^- \rightarrow 0$ as $x \rightarrow -\infty$. Matching at the bubble tip requires that $h^+=h^-$ and $h_{,x}^\pm \rightarrow \infty$, so that $C^+=C^-$ and then Eqs. (A3) and (A4) imply that

$$\Delta p(1 - h_0) + 1/2Bo(1 - h_0^2) = 2. \quad (\text{A6})$$

Using Eq. (A5) to eliminate Δp in Eq. (A6) gives a quadratic equation for h_0 with the solutions

$$h_0 = 1 \pm 2/\sqrt{Bo}.$$

Discarding the solution that lies outside the channel gives $h_0 = 1 - 2/\sqrt{Bo}$ and so the dimensionless width of the bubble is $2/\sqrt{Bo}$. Note that when $Bo < 1$ the width of the bubble exceeds the width of the channel and so the solution is invalid.

APPENDIX B: RIGID-WALL SIMULATIONS

Air finger propagation in a rigid channel under the influence of transverse gravity is a special case of the model problem described in Sec. II. The walls are fixed at $x_2=-1$ and $x_2=1$, and there is no longer flux constraint (11) on the system. Boundary conditions (10) and (11) far ahead of the finger tip are replaced by the conditions $u_2=0$ and $p=-Bo/Ca x_2$, which specify purely axial flow and set a reference fluid pressure. The latter is required because the external pressure does not affect the system when the channel walls are rigid.

In rigid geometries, accurate results can be obtained in much shorter domains than in the elastic case. We choose $-6 \leq x_1 \leq 5$, and the consequent increase in the spatial resolution for our standard mesh means that we can simulate the

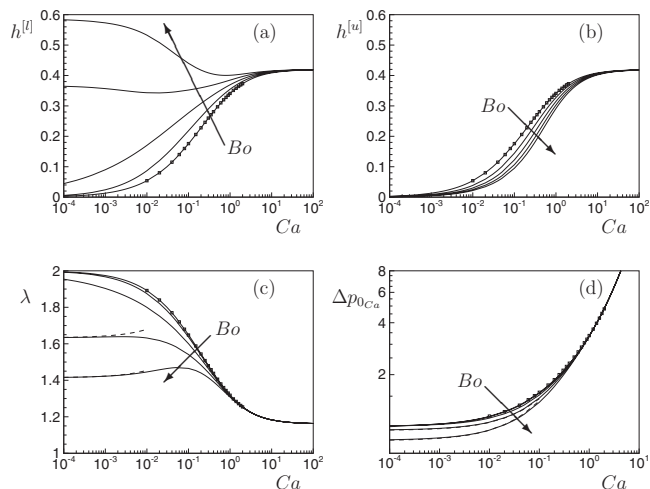


FIG. 12. The behavior of an air finger propagating at constant speed into a rigid channel under the influence of a gravitational body force acting perpendicularly to the channel's axis. Results are shown for Bond numbers $Bo = \rho g H^2 / \gamma^* = 0, 0.5, 1, 1.5,$ and 2 , increasing in the direction of the arrows. We present the (a) dimensionless height of the lower fluid film $h^{[l]} = h^{[l]s} / H$, (b) dimensionless height of the upper fluid film $h^{[u]} = h^{[u]s} / H$, and (c) dimensionless width of the finger $\lambda = W_b^* / H = 2 - h^{[u]} - h^{[l]}$, all evaluated at the end of our domain, $x_1 = -6$. We also present (d) the pressure drop across the interface at the centerline of the channel on the capillary scale $\Delta p_{0,Ca} = [p_b^* - p_{fluid}^*(x_2=0)] / (\gamma^* / H)$. The data of Reinelt and Saffman (Ref. 23) for $Bo=0$ are shown as open squares and the asymptotic results of Jensen *et al.* (Ref. 21) for $Bo > 1$ and $Ca \ll 1$, Eqs. (B1b) and (B1c), are shown as dashed lines in (c) and (d).

range $10^{-4} \leq Ca \leq 100$. In the absence of gravity ($Bo=0$) our results are in agreement with the calculations of Reinelt and Saffman²³ to within an accuracy of 0.4%. Typical results for zero fluid inertia, $Re=0$, and $Bo=0, 0.5, 1, 1.5,$ and 2 are presented in Fig. 12 which shows the thickness of the fluid films and the width of the finger far behind the finger tip (at $x_2=-6$), together with the pressure drop across the interface at the channel's centerline, $x_2=0$.

The effects of gravity are most pronounced at low capillary numbers (low propagation speeds), where the viscous forces are relatively weak and the dominant balance is between gravitational and surface-tension forces. Increasing the Bond number causes a buoyant rise of the finger, decreasing the upper-film thickness $h^{[u]}$, increasing the lower-film thickness, $h^{[l]}$, and decreasing the overall width of the finger, λ , as it rises toward the upper wall. Note the dramatic reduction in finger width once $Bo > 1$, a regime in which the static ($Ca=0$) solution no longer touches the lower wall, see Appendix A. The interfacial pressure drop at the channel's centerline is approximately independent of the Bond number for $Bo \leq 1$ but then decreases with increasing the Bond number because the interfacial curvature at $x_2=0$ decreases when the finger rises.

The asymptotic predictions of Jensen *et al.*²¹ are valid when $Ca/|1-Bo| \ll 1$, and when $Bo=1.5$ and 2 , our numerical results for the pressure drops and finger widths approach the $Bo > 1$ predictions of Jensen *et al.*²¹ as $Ca \rightarrow 0$:

$$h^{[u]} \sim \frac{1.3375 Ca^{2/3}}{2\sqrt{Bo}}, \quad h^{[l]} \sim 2 - \frac{2 + 1.9 Ca^{2/3}}{\sqrt{Bo}}, \quad (\text{B1a})$$

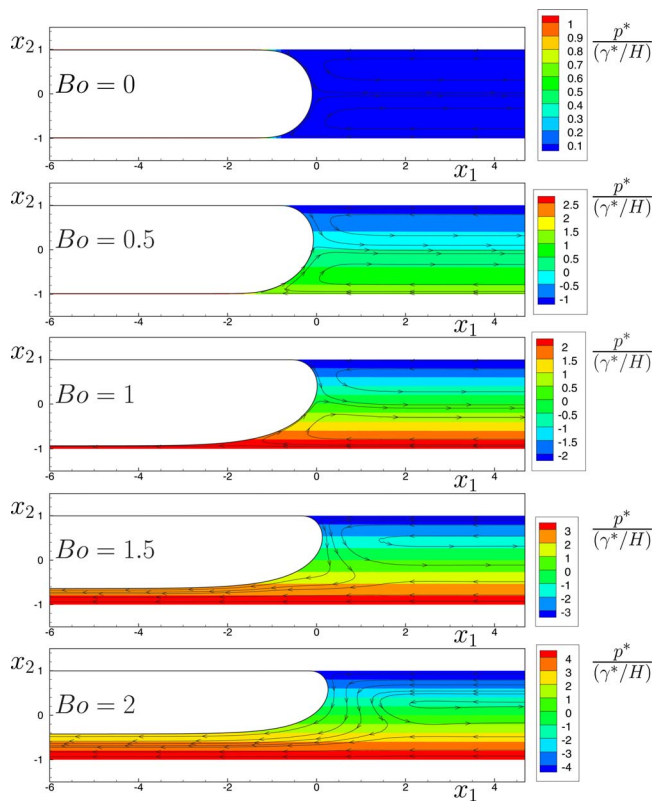


FIG. 13. (Color online) Contours of fluid pressure and streamlines for an air finger propagating at a constant speed into a rigid channel at a fixed capillary number, $Ca=0.001$, for Bond numbers $Bo=0, 0.5, 1, 1.5$, and 2 .

$$\lambda = 2 - h^{[u]} - h^{[l]} \sim \frac{2 + 1.23125 Ca^{2/3}}{\sqrt{Bo}}, \quad (\text{B1b})$$

$$\Delta p_{0Ca} \sim 2\sqrt{Bo} - Bo + 1.9\sqrt{Bo} Ca^{2/3}. \quad (\text{B1c})$$

These asymptotic expressions are shown by the dashed lines in Figs. 12(c) and 12(d). The discrepancy between the numerical and asymptotic predictions for λ remains below 1% for $Ca \leq 0.003$ when $Bo=1.5$ or $Ca \leq 0.015$ when $Bo=2$, indicating the increasing accuracy of the approximation as Bo increases. For $Bo < 1$, the predictions of Jensen *et al.*²¹ for the film thicknesses and pressure drop are

$$h^{[u]} \sim \frac{1.3375 Ca^{2/3}}{1 + \sqrt{Bo}}, \quad h^{[l]} \sim \frac{1.3375 Ca^{2/3}}{1 - \sqrt{Bo}},$$

$$\Delta p_{0Ca} \sim 1 + 3.8 Ca^{2/3},$$

which reduce to the well-known Bretherton⁶ formulas for $Bo=0$. When $Bo=0.5$ and 1 , our numerical results approach the predictions for $h^{[u]}$ and Δp_{0Ca} as $Ca \rightarrow 0$ (not shown). The prediction for $h^{[l]}$ diverges as $Bo \rightarrow 1$ and although the differences between the prediction and simulation decrease as $Ca \rightarrow 0$, the discrepancy between the two is approximately 75% at $Bo=0.5$ when $Ca=10^{-4}$. Thus the predictions for the finger widths for $0.5 \leq Bo < 1$ will be accurate only at extremely small capillary numbers.

In all cases as the capillary number increases the results become independent of the Bond number, a consequence of

functional form Bo/Ca appearing in the governing equations (1). In physical terms viscous forces dominate the behavior of the system and the relevant balance is between the viscous and surface-tension forces. The pressure drop and finger width are essentially independent of the Bond number for $Ca \geq 1$ (relative differences less than 0.8%), but the relative differences in thicknesses of the fluid films do not fall below 1% until $Ca \geq 20$. In other words, the shape of the finger remains essentially unchanged for $Ca \geq 1$, but the finger does not become centered within the channel until $Ca \geq 20$.

Figure 13 shows streamlines and contours of the fluid pressure on the surface-tension scale for $Ca=0.001$ over a range of Bond numbers $Bo=0, 0.5, 1, 1.5$, and 2 . As the Bond number increases the development of a significant transverse pressure gradient can be seen. The capillary number is small enough that the interface shape is close to the static configuration and for $Bo \geq 1$, the development of a non-negligible lower film can be seen. By $Bo=1.5$, a single recirculation region replaces the two that are present in the absence of gravity.

¹E. J. Burger, Jr. and P. Macklem, "Airway closure: Demonstration by breathing 100% O₂ at low lung volumes and by N₂ washout," *J. Appl. Physiol.* **25**, 139 (1968).

²N. B. Pride and P. T. Macklem, "Lung mechanics in disease," in *Handbook of Physiology: The Respiratory System* (American Physiological Society, Bethesda, MD, 1986), Vol. III, Sec. III, pp. 659–692.

³J. B. Grotberg, "Pulmonary flow and transport phenomena," *Annu. Rev. Fluid Mech.* **26**, 529 (1994).

⁴D. P. Gaver III, R. W. Samsel, and J. Solway, "Effects of surface tension and viscosity on airway reopening," *J. Appl. Physiol.* **369**, 74 (1990).

⁵D. P. Gaver III, D. Halpern, O. E. Jensen, and J. B. Grotberg, "The steady motion of a semi-infinite bubble through a flexible walled channel," *J. Fluid Mech.* **319**, 25 (1996).

⁶F. P. Bretherton, "The motion of long bubbles in tubes," *J. Fluid Mech.* **10**, 166 (1961).

⁷A. L. Hazel and M. Heil, "Three-dimensional airway reopening: The steady propagation of a semi-infinite bubble into a buckled elastic tube," *J. Fluid Mech.* **478**, 47 (2003).

⁸D. Y. K. Yap and D. P. Gaver III, "The influence of surfactant on two-phase flow in a flexible-walled channel under bulk equilibrium conditions," *Phys. Fluids* **10**, 1846 (1998).

⁹M. Heil, "Finite Reynolds number effects in the propagation of an air finger into a liquid-filled flexible-walled tube," *J. Fluid Mech.* **424**, 21 (2000).

¹⁰S. Naire and O. E. Jensen, "Epithelial cell deformation during surfactant-mediated airway reopening: A theoretical model," *J. Appl. Physiol.* **99**, 458 (2005).

¹¹D. Halpern, S. Naire, O. E. Jensen, and D. P. Gaver III, "Unsteady bubble propagation in a flexible channel: Predictions of a viscous stick-slip instability," *J. Fluid Mech.* **528**, 53 (2005).

¹²A. Juel and A. Heap, "The reopening of a collapsed fluid-filled elastic tube," *J. Fluid Mech.* **572**, 287 (2007).

¹³A. L. Hazel and M. Heil, "Finite-Reynolds-number effects in three-dimensional airway reopening," *ASME J. Biomech. Eng.* **128**, 573 (2006).

¹⁴G. A. Wempner, *Mechanics of Solids* (McGraw-Hill, New York, 1973).

¹⁵M. Heil and A. L. Hazel, "oomph-lib: An object-oriented multi-physics finite-element library," in *Fluid-Structure Interaction*, Lecture Notes on Computational Science and Engineering, edited by M. Schafer and H.-J. Bungartz (Springer, New York, 2006).

¹⁶P. M. Gresho and R. L. Sani, *Incompressible Flow and the Finite Element Method, Vol. 2, Isothermal Laminar Flow* (Wiley, Chichester, England, 2000).

¹⁷S. F. Kistler and L. E. Scriven, "Coating flows," in *Computational Analysis of Polymer Processing*, edited by J. R. A. Pearson and S. M. Richardson (Applied Science, London, 1983), pp. 243–299.

- ¹⁸K. J. Ruschak, "A method for incorporating free boundaries with surface tension in finite element fluid-flow simulators," *Int. J. Numer. Methods Eng.* **15**, 639 (1980).
- ¹⁹M. L. Perun and D. P. Gaver III, "Interaction between airway lining fluid forces and parenchymal tethering during pulmonary airway reopening," *J. Appl. Physiol.* **79**, 1717 (1995).
- ²⁰Y. Zheng, H. Fujioka, and J. B. Grotberg, "Effects of gravity, inertia, and surfactant on steady plug propagation in a two-dimensional channel," *Phys. Fluids* **19**, 082107 (2007).
- ²¹M. H. Jensen, A. Libchaber, P. Pelcé, and G. Zocchi, "Effect of gravity on the Saffman–Taylor meniscus: Theory and experiment," *Phys. Rev. A* **35**, 2221 (1987).
- ²²O. E. Jensen, M. Horsburgh, D. Halpern, and D. P. Gaver III, "The steady propagation of a bubble in a flexible-walled channel: Asymptotic and computational models," *Phys. Fluids* **14**, 443 (2002).
- ²³D. A. Reinelt and P. G. Saffman, "The penetration of a finger into a viscous fluid in a channel and tube," *SIAM (Soc. Ind. Appl. Math.) J. Sci. Stat. Comput.* **6**, 542 (1985).